Article:

Li, Zhenyu and Bors, Adrian Gheorghe orcid.org/0000-0001-7838-0021 (2020) Steganalysis of meshes based on 3D wavelet multiresolution analysis. Information Sciences. pp. 164-179. ISSN 0020-0255

https://doi.org/10.1016/j.ins.2020.02.061

Steganalysis of Meshes Based on 3D Wavelet multiresolution Analysis

Zhenyu Li, Adrian G. Bors[*]

Department of Computer Science, University of York, York YO10 5GH, UK

Abstract

3D steganalysis aims to find the information hidden in 3D models and graphical objects. It is assumed that the information was hidden by 3D steganography or watermarking algorithms. A new set of 3D steganalysis features, derived by using multiresolution 3D wavelet analysis, is proposed in this research study. 3D wavelets relate a given mesh representation with its lower and higher graph resolutions by means of a set of Wavelet Coefficient Vectors (WCVs). The 3D steganalysis features are derived from transformations between a given mesh and its corresponding higher and lower resolutions. They correspond to geometric measures such as ratios and angles between various geometric measures. These features are shown to significantly increase the steganalysis accuracy when detecting watermarks which have been embedded by 3D wavelet-based watermarking algorithms. The proposed features, when used in combination with a previously proposed feature set, is shown to provide the best results in detecting the hidden information embedded by other information hiding algorithms.

Keywords: 3D steganalysis, 3D wavelets, multiresolution analysis, information hiding, feature spaces.

1. Introduction

3D meshes are one of the most common representations for surfaces of objects in computer graphics and computer vision [1]. Due to their simplicity of representation and low memory requirements, 3D meshes are used in many applications, including virtual reality, augmented reality, 3D printing models, medical imaging, digital heritage representations, computer aided design and so on. With the development of specialized systems for 3D object scanning and representation, 3D models are becoming more and more widespread while being also accessible to the general public. Meanwhile, processing algorithms such as 3D information hiding algorithms are increasingly used in various situations, including for covert communication, information storage and subsequent retrieval, copyright protection, among many others.

Steganalysis is the counterpart to information hiding, aiming to detect the embedded information in a given data representation structure. Steganalysis is extremely important for identifying the information which was unlawfully embedded. Steganalysis can also be used to detect the executable code or the URL containing an internet address, embedded in a digital file, which can be used by malware programs, such as Stegoloader [2] and Lurk Downloader [3], for malicious attacks. Furthermore, 3D steganalysis can contribute to the development of robust 3D information hiding algorithms [4], by being used for testing the detectability of the embedded information.

During the last two decades, 3D information hiding methodology has expanded significantly. 3D information hiding algorithms can be classified into two categories, according to the domain used for embedding information: spatial and transformed. In the context of the spatial domain methods, the first two 3D information hiding algorithms were proposed by Ohbuchi *et al.* in [5] by considering ratios of local geometric

---

[*] Corresponding author

Email addresses: `zheenyuli@gmail.com` (Zhenyu Li), `adrian.bors@york.ac.uk` (Adrian G. Bors)

measurements. Later, Cayre and Macq [6] proposed a 3D steganographic approach which embeds information in each triangle of the mesh by considering it as a two-state binary code corresponding to either a 1 or a 0. Two blind robust 3D watermarking algorithms modifying either the mean or the variance for the radius of vertices, when represented in the spherical coordinate system, were proposed by Cho *et al.* [7]. A watermarking algorithm that changes the statistics of geodesic distances calculated from a particular point on the surface of the 3D object, was proposed by Luo and Bors [8]. The same authors also proposed a 3D watermarking which ensures a minimal surface distortion by using an optimization algorithm in [9]. More recently, in order to improve the anti-steganalytic properties of the watermarking algorithms from [7], Yang *et al.* [10] proposed a Steganalysis-Resistant Watermarking (SRW) algorithm, embedding information by changing the heights of the histogram bins for the radial coordinates of the vertices. Meanwhile, high capacity 3D information hiding algorithms have also been developed. For example, Multi-Layer Steganography (MLS) [11] can embed information into 3D objects by using the vertices' projections onto the principal axis of the object. This method can embed a payload as high as 10 Bits Per Vertex (BPV). Additionally, inspired by [12], Itier *et al.* [13] proposed a 3D steganography based on the Hamiltonian Path Quantization (HPQ) which can embed 3 BPV. Moreover, Itier *et al.*, in the research study from [14] improved the embedding capacity using HPQ to 24 BPV while using the static arithmetic coding during the embedding. An algorithm which embeds changes into 3D objects, that cannot be found by the existing 3D steganalysis algorithms at that time, was proposed in [4]. This approach is called HPQ-R and represents an extension of the HPQ [14] algorithm by modifying the radial component of the spherical coordinate system, defined in a localized area.

The 3D wavelet domain is the most popular transform domain used for 3D information hiding because it allows to embed information into 3D objects at multiple scales of representation. 3D wavelet multiresolution analysis, introduced in [15], provides a multiresolution analysis framework for 3D shapes. Under this framework, a given mesh is represented by a coarser mesh and a set of vectors, called Wavelet Coefficient Vectors (WCV), used for encoding the details. 3D wavelet analysis was used for various applications including filtering [16], mesh compression [17, 18], subdivision [19], as well as information hiding [20, 21, 22, 23, 24, 25]. A 3D wavelet-based watermarking algorithm was proposed by Kanai *et al.* [20], which modifies the ratio between the norm of a WCV and the length of its support edge. However, this 3D watermarking method is not blind, which significantly reduces its potential for application. Uccheddu *et al.* [21] proposed a blind 3D wavelet-based watermarking algorithm that embeds information by changing the position of the WCV's terminal point, according to a watermarking map generated by a secret key. Kim *et al.* proposed two watermarking methods in [22] and in [23], by extending the approach from [7], both methods embedding changes in the bins of the histogram representing WCVs' norms. A hierarchical 3D watermarking methodology based on the wavelet transform was developed by Wang *et al.* [24], which includes three different algorithms, each one enforcing one of the following requirements: robustness, high-capacity and fragility for authentication. Zaid *et al.* [25] proposed a high-capacity 3D wavelet-based watermarking algorithm, by applying Quantization Index Modulation (QIM) [26] on the WCVs in order to embed information. More details about the 3D wavelet-based information hiding algorithms are given in Section 2.

A particular class of information hiding methods can achieve high embedding capacities while producing very small changes to the 3D objects. An example of this category is the fragile watermarking proposed in [24]. Other 3D information hiding algorithms would embed information by changing the order of vertices in the mesh representation, by using permutations for example, resulting in no surface changes. Examples of such methods are those described in [27, 28, 29]. However, such watermarks can be found when a third party would find the reference vertex while the ordering algorithm is known because it is public.

While the application of steganalysis in the image and audio domains has received significant attention from the research community, research into 3D steganalysis is still in its infancy. 3D steganalysis is more challenging than the image or audio steganalysis, because 3D objects are characterized by additional complexity when compared to the lower dimensional data such as images or audio signals. The geometry of 3D objects is mostly irregular, which is totally different from the rectangular grid alignment for image pixels or the regular time sampling of audio signals. The application of image or audio steganalytic algorithms to 3D watermarked objects would not lead to useful results under these circumstances.

Yang and Ivrissimtzis [30] proposed a 3D steganalytic approach using the quadratic classifier and the 208-dimensional feature vector, called YANG208, characterizing the norms of vertices in the Cartesian and Laplacian coordinate systems [31], the dihedral angle of faces adjacent to the same edge, and the face normal, for 3D stegnalalysis. Li and Bors [32] improved the YANG208 feature set by preserving the efficient feature subset and adding the vertex normal and curvature features, forming the Local Feature Set (LFS52). Kim *et al.* [33] proposed LFS64, which includes LFS52 and features representing the edge normal, mean curvature and total curvature. Meanwhile, Li and Bors [34] extended LFS52 to LFS76 by adding the 24 dimensional features extracted from the spherical coordinate system representation of vertices and edges. The same authors proposed in [35] a feature selection algorithm designed to address the cover source mismatch problem in 3D steganalysis, by considering the features' robustness to the variation of cover sources.

The performance of existing 3D steganalytic approaches, such as the ones proposed in [30, 32, 34], is rather poor when attempting to detect messages hidden by 3D wavelet-based watermark embedding algorithms, according to the results from [34]. In this research study we propose to use the 3D wavelet domain which provides a different framework for mesh representation, by defining relationships between meshes at different scales. The best feature detection is usually achieved by using feature extractors that match those used when embedding the information, as it has been considered for image steganalysis in [36, 37]. Given that the embedding domain of 3D wavelet-based watermarking algorithms is known, we can extract relevant features from the same domain in order to capture the distortions corresponding to embeddings. 3D wavelet features, derived from the 3D wavelet domain are extracted from the original mesh and its smoothed version for various resolution levels. Such features model the characteristics of the 3D object transformations from one scale representations to another. Empirical probability density functions (PDFs) of the logarithm of differences between the features extracted from either the stego-meshes or the cover-meshes and from their smoothed counterparts are then formed. The first four moments of these PDFs are then used to form a 228-dimensional feature vector which is eventually fed into a classifier. Following training, the classifier discriminates stego-objects from cover-objects based on the statistical properties of the 3D wavelet feature set.

The rest of this paper is structured as follows: Section 2 describes the procedure for information hiding in the 3D wavelet domain. The 3D steganalysis framework is described in Section 3. The approach for extracting the 3D wavelet feature set using multiresolution mesh analysis is presented in Section 4. The experimental results are provided in Section 5, while this paper is concluded in Section 6.

2. Information hiding in the 3D wavelet domain

In this section, we describe the 3D wavelet decomposition mechanism and then explain how information can be embedded in this representation. At each iteration of the 3D wavelet decomposition, the mesh is decomposed into a coarser mesh representation and a set of Wavelet Coefficient Vectors (WCVs). Then, the 3D wavelet decomposition continues recursively, until the mesh obtained cannot be decomposed any further. Fig. 1 illustrates an iteration of the lazy wavelet decomposition, [15]. The decomposition is applied on meshes consisting of triangles, while other polygons can be easily decomposed in sets of triangles. For illustrative purposes we consider four triangles, including one in the center surrounded by three others, as shown in Fig. 1. During the 3D wavelet decomposition, the three vertices, defining the central triangle, are removed, while the remaining three vertices would form a new triangle. Consequently, following the 3D wavelet decomposition, the four original triangles are transformed into a single triangle, part of a coarser mesh. At the same time, three WCVs are obtained as the vectors from the midpoints of the new edges to the vanished vertices. The new edges in the larger triangle are called the support edges for the WCVs. The new larger triangle preserves the basic shape formed by the former four triangles while the WCVs would encode the local details of the 3D shape. This decomposition propagates on the whole mesh generating a coarser mesh together with a set of WCVs. The mathematical formulation defining the 3D wavelet decomposition and more details about the procedure of the decomposition can be found in [15].

In the following we discuss the watermarking method of Wang *et al.* [24], as being a representative 3D wavelet-based information hiding algorithm which changes both the norms and the directions of the WCVs. After recursively applying the 3D wavelet decomposition several times, a series of meshes at various scales and their corresponding sets of WCVs are generated. The hierarchical watermarking method proposed in

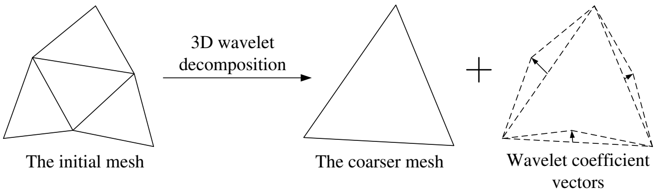

Figure 1: Example when applying 3D wavelet decomposition on triangle meshes.

[24] can be used to embed three different types of watermarks into the WCVs: one which is robust, a second of high capacity, and another one which embeds fragile watermarks. A robust watermark is embedded by modifying the norms of the WCVs associated with the lowest resolution level of the mesh. Then, a denser mesh is reconstructed based on the lowest resolution mesh and its corresponding watermarked WCVs. For embedding the high capacity watermark code, at each iteration, the WCVs are indexed according to the lengths of their support edges for synchronization. A parameter p, representing the quantization step used in the high capacity watermarking, is calculated as $p = l_{av}/\epsilon_{hc}$, where l_{av} is the average length of the WCVs' support edges, and ϵ_{hc} is a controlling parameter. The watermark is embedded by adjusting the residuals, of the WCVs' norms divided by the parameter p, into a certain sequence. Finally, the fragile watermark is embedded before the last iteration of the mesh reconstruction. In the case of the fragile watermark embedding, an identical symbol is embedded by two different embedding approaches. One approach is based on the quantization of the angle between the WCV and its support edge using the M-symbol scalar Costa scheme [38], which depends on a quantization step Δ_θ. In the second embedding approach, the symbol is embedded by adjusting the norm-length ratio of the WCV and its support edge. Finally, the hierarchically watermarked mesh is reconstructed to its initial mesh size.

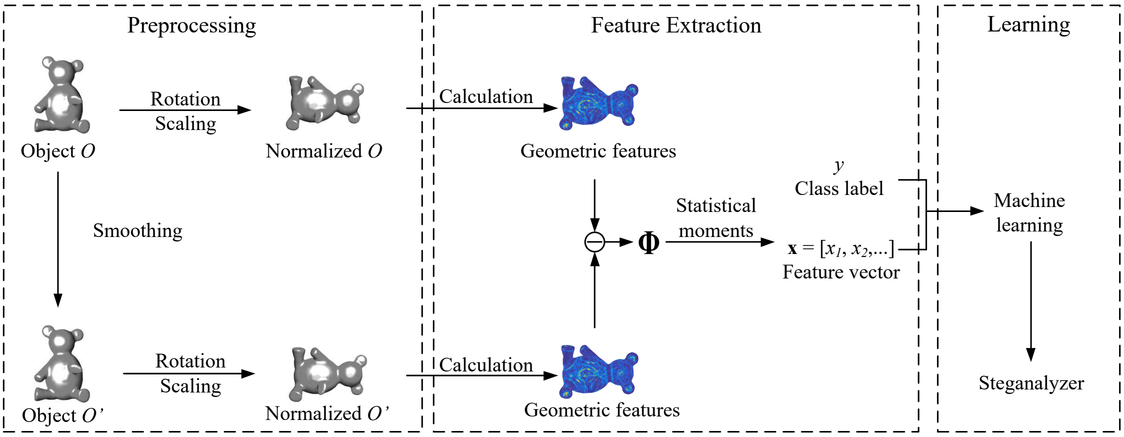

Figure 2: The 3D steganalysis framework based on learning from the 3D wavelet feature statistics followed by classification into stego-objects and cover-objects.

3. The 3D steganalysis framework

In the following we briefly discuss the 3D steganalysis framework. A steganalyzer learns to discriminate stego-objects from cover-objects, which represent objects carrying hidden information from those not not carrying, respectively. Steganalysis can be treated as a supervised learning problem consisting of training and testing stages. Training a 3D steganalyzer is illustrated in Fig. 2 and has the following processing steps: data pre-processing, feature extraction and learning. During the testing stage, the characteristic feature set is extracted from a given set of objects, and the steganalyzer, whose parameters had been learnt during the training stage, is used to discriminate stego-objects from cover-objects.

Let us assume that we have a 3D object $\mathcal{O} = \{V, F, E\}$, $V = \{v_i | i = 1, 2, \ldots, |V|\}$ representing the vertex set, where $|V|$ is the number of vertices in the object $\mathcal{O}$, while F and E represent its face and edge sets, respectively. During the pre-processing stage, Laplacian smoothing is performed on the object $\mathcal{O}$, which is a similar operation to the "calibration" technique used in image steganalysis, [39]. A scale parameter λ, defined empirically, is used to control the smoothing degree. Then the original object $\mathcal{O}$ and its smoothed version $\mathcal{O}'$, are rotated and scaled such that they are constrained within a cube with sides of length 1. It would be expected that the difference between $\mathcal{O}$ and its smoothed version $\mathcal{O}'$ is larger when $\mathcal{O}$ is a stego-object than in the case when $\mathcal{O}$ is a coverobject.

The 3D features used for steganalysis are chosen according to their geometrical characteristics in discriminating stego-objects from cover-objects. As mentioned in Section 1, statistics of various features have been proposed for 3D steganalysis in [30, 32, 33, 34]. The most important difference between the approach proposed in this paper from other 3D steganalysis approaches is that by using the 3D wavelet analysis framework we extract features modelling transitions between 3D object representations at different scales. Differences between the geometric features from the original object and its smoothed version are computed, forming a set $\mathbf{\Phi}$. Then, the steganalysis feature vector is made up from the first four statistical moments of the logarithm of $\mathbf{\Phi}$. A large number of steganalysis feature vectors are extracted from both cover-objects and their corresponding stego-objects. These are then used as inputs for a machine learning algorithm such as the Fisher Linear Discriminant (FLD) ensemble which was used in [34] as well.

4. Extracting 3D wavelet features using multiresolution mesh analysis

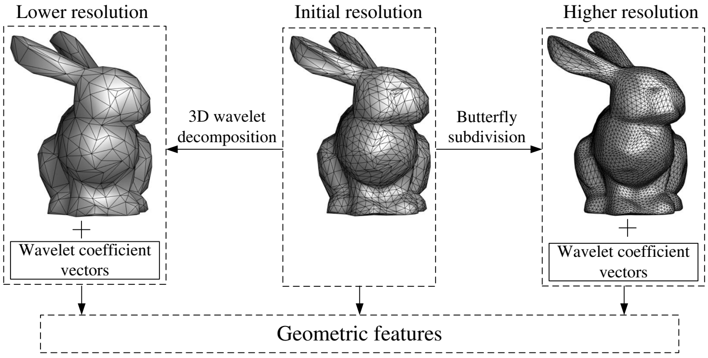

Figure 3: Generating multiresolution meshes using the 3D wavelet decomposition and Butterfly subdivision.

3D wavelet decompositions provide a transformation between the scales of meshes for a 3D object. The Wavelet Coefficient Vectors (WCVs), which are produced following the 3D wavelet decomposition encode essential information about the 3D shape of the object. In this section we firstly provide an outline of the 3D wavelet analysis methodology and how this can be applied for extracting features which are useful for steganalysis. Fig. 3 illustrates how, by using 3D wavelet analysis, the original object $\mathcal{O}$ is decomposed into a lower resolution mesh $\mathcal{O}^l$, and WCVs, shown to the left, by using the 3D lazy wavelet decomposition [15]. The same mesh is subdivided, as shown in the right side of Fig. 3, into a higher resolution mesh $\mathcal{O}^h$ and the corresponding WCVs, using the Butterfly scheme [40]. Geometric features, which are then used for steganalysis, are generated using the initial resolution mesh, the lower resolution, the higher resolution, and the corresponding WCVs, resulting from the processes of down-scaling or up-scaling the 3D object.

Most of 3D wavelet-based watermarking approaches modify the WCVs and their corresponding edges from the lower resolution of the mesh in order to hide information into the 3D mesh. This motivated us to find characteristic features from the lower resolution meshes and their corresponding WCVs and use them for steganalysis. Meanwhile, the vertices from the higher resolution mesh are obtained from the corresponding larger neighborhood of vertices from the original mesh. This indicates that the geometric features from the higher resolution mesh are likely to be more sensitive to the changes in the original mesh. The features that we will use for steganlysis are extracted based on the transformations of both up-scaling and down-scaling the given mesh and the corresponding WCVs. In the following we provide the methodology for extracting the proposed steganalysis features by means of the 3D wavelet multiresolution analysis framework.

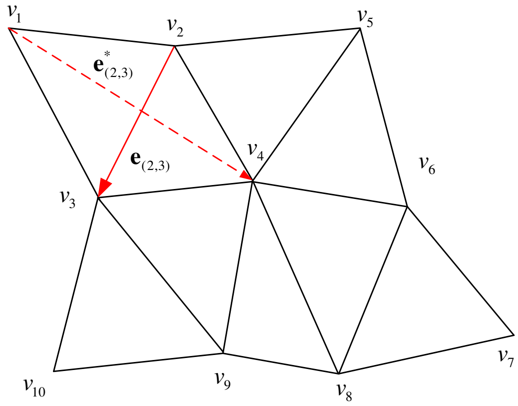

Figure 4: Extracting edge vectors and their flipped counterparts from the mesh of initial resolution.

4.1. Extracting geometric features from the initial mesh

The first two geometric features, considered in this research study, are extracted from the initial mesh and represent the edge vector and its corresponding flipped edge vector. The edge vectors $\{\mathbf{e}_{(i,j)}\}$ represent the vectors from the vertex v_i to the vertex v_j, where v_i and v_j are adjacent in the initial resolution mesh. An example of edge vector is illustrated in Fig. 4 as $\mathbf{e}_{(2,3)}$. Each flipped edge vector $\{\mathbf{e}^*_{(i,j)}\}$ is connecting the opposite vertices, from the triangles which are sharing the associated edge vector $\{\mathbf{e}_{(i,j)}\}$. For example, the vector $\mathbf{e}^*_{(2,3)}$ from Fig. 4, connecting two vertices v_1 and v_4, is the flipped edge vector of the edge vector $\mathbf{e}_{(2,3)}$. The direction of the flipped edge vector is oriented from the vertex with a lower index to the one with a higher index, as shown in Fig. 4.

4.2. Geometric features extracted from the lower resolution mesh

The lower resolution mesh is obtained after one iteration of the 3D lazy wavelet decomposition, which is illustrated in Fig. 5. In this figure, four triangles $\triangle v_4v_5v_6, \triangle v_4v_6v_8, \triangle v_6v_7v_8$ and $\triangle v_4v_8v_9$ from the initial resolution mesh are merged into a single larger triangle $\triangle v_5v_7v_9$ as part of a coarser mesh at a lower resolution of surface representation. The vertices, v_4, v_6 and v_8 in Fig. 5 corresponding to the terminal points for the three WCVs, $\mathbf{w}^l_{(5,9)}$, $\mathbf{w}^l_{(5,7)}$ and $\mathbf{w}^l_{(7,9)}$, are removed while down-scaling the mesh. The subscripts of $\mathbf{w}^l_{(i,j)}$ represent the two vertices v_i and v_j of the WCV's support edge $\mathbf{e}^l_{(i,j)}$ from the lower resolution mesh. Meanwhile, the initial point of the WCV, $\mathbf{w}^l_{(5,9)}$, is the midpoint of its support edge $\mathbf{e}^l_{(5,9)}$ in the lower resolution mesh. Consequently, each edge vector from the lower resolution mesh is associated with one WCV. $\mathbf{w}^l_{(i,j)}$ and the edge vector, $\mathbf{e}^l_{(i,j)}$, from the lower resolution mesh representation are considered as components of the proposed 3D wavelet feature vector used for steganalysis. The reason we have chosen these WCVs and their support edge vectors as steganalytic features is because these are changed when hiding information by the steganographical algorithms proposed in [20, 24, 25].

Two other features are considered from the lower resolution mesh. The first is represented by the angle between the WCV and its support edge vector in the lower resolution mesh, defined as

$$\alpha_{(i,j)} = \arccos\left(\frac{\mathbf{w}^{\mathrm{l}}_{\mathrm{(i,j)}} \cdot \mathbf{e}^{\mathrm{l}}_{\mathrm{(i,j)}}}{\|\mathbf{w}^{\mathrm{l}}_{\mathrm{(i,j)}}\| \cdot \|\mathbf{e}^{\mathrm{l}}_{\mathrm{(i,j)}}\|}\right), \tag{1}$$

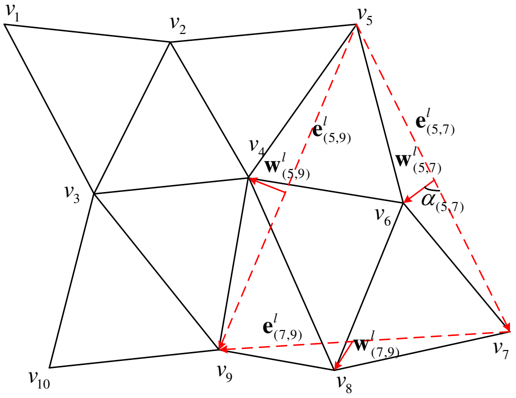

Figure 5: The illustration of the 3D wavelet decomposition for a mesh down-scaling from its original resolution to a lower resolution.

where i and j are the indices of two adjacent vertices in the lower resolution mesh. For example, as illustrated in Fig. 5, $\alpha_{(5,7)}$ is the angle between $\mathbf{w}^l_{(5,7)}$ and its support edge vector, $\mathbf{e}^l_{(5,7)}$. The other one is the ratio between the Euclidean norm of the WCV and that of its support edge vector in the lower resolution mesh, defined as

$$\rho^l_{(i,j)} = \frac{\|\mathbf{w}^l_{(i,j)}\|}{\|\mathbf{e}^l_{(i,j)}\|}. \tag{2}$$

These two geometric features are used to carry information payloads in various 3D wavelet watermarking methods such as those proposed in [24, 41] and this is the reason why they are also considered in our 3D staganalytic method.

One important aspect when considering the 3D wavelet decomposition is that the steganalyst may not be able to know what set of triangle faces had been grouped when the information was embedded into the 3D shape. In fact, the grouping of the triangle faces determines how the WCVs are produced. For instance, in Fig. 5, if the four triangles $\triangle v_2v_3v_4, \triangle v_3v_4v_9, \triangle v_4v_8v_9$ and $\triangle v_3v_9v_{10}$ would merge into a larger triangle $\triangle v_2v_8v_{10}$ in the lower resolution mesh, we would not be able to retrieve certain WCVs, such as $\mathbf{w}^l_{(5,9)}$ and $\mathbf{w}^l_{(7,9)}$. By not knowing this information, we can have a mismatch of the 3D wavelet decompositions which would degrade the performance of the steganalysis. In order to mittigate this problem we consider all possible groupings for the triangle faces in the given neighborhood, generating all the possible WCVs together with their support edge vectors in the lower resolution meshes. In consequence, we define all groups of four neighboring triangles including one triangle in the centre, surrounded by the other three triangles, that can be merged into a larger triangle during the 3D wavelet decomposition. Since each triangle from a fully connected mesh can be the central triangle used in 3D wavelet decomposition, we can obtain $|F|$ different groups of four neighboring triangles, where $|F|$ is the number of the triangles from the initial resolution mesh. For each of these triangle groupings, we apply the 3D wavelet decomposition and calculate the geometric features as described before in this section. Meanwhile, we remove the duplicated geometric features, such as the WCVs and edge vectors which are generated more than once when considering all triangle groupings. Finally, the resulting features, considering all the possible grouping options in the wavelet decomposition, form the geometric features from the lower resolution mesh.

4.3. Geometric features extracted from the higher resolution mesh

When transforming the given mesh into a higher resolution mesh, each triangle from the original resolution mesh is subdivided into four smaller triangles by inserting three new vertices, each located on one of the edges from the initial resolution triangle. In the higher resolution mesh, each newly inserted vertex is adjacent to the two ends of the support edge of the initial resolution triangle while it is also adjacent to the other newly inserted vertices. As illustrated in Fig. 6, the vertices $v_{11}, v_{12}, v_{13}, v_{14}$ and v_{15} are added to the

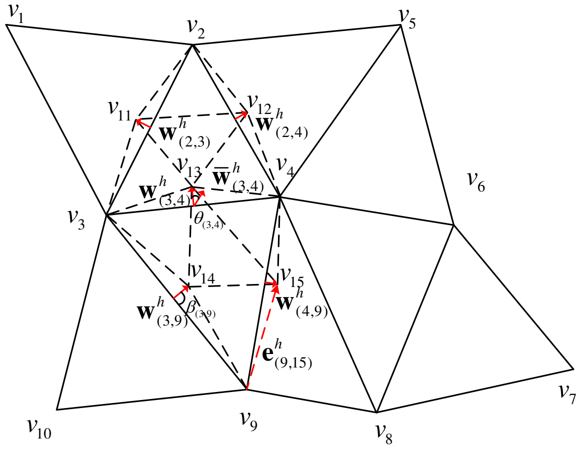

Figure 6: Illustration of the 3D wavelet subdivision when the mesh is transformed from the original resolution to a higher resolution.

local mesh in order to produce the higher resolution mesh following the 3D wavelet transformation. Since the subdivision is based on the Butterfly scheme [40], the position of each newly added vertex is computed from eight vertices which define a neighborhood resembling the shape of a butterfly. We apply one iteration subdivision using the Butterfly scheme with the tension parameter $\omega = \frac{1}{16}$, as in [17, 40]. When $\omega \to 0$, the surface of the 3D object becomes more like that of a piecewise linear polyhedron. The tension parameter characterizes the smoothness and for $\omega = \frac{1}{16}$ the resulting surface has globally $\mathbf{C}^1$ continuity. For example, the position of the vertex v_{13} associated to edge vector $\mathbf{e}_{(3,4)}$ in Fig. 6 is given by :

$$v_{13} = \frac{1}{2}(v_3 + v_4) + \frac{1}{8}(v_2 + v_9) - \frac{1}{16}(v_1 + v_5 + v_8 + v_{10}). \tag{3}$$

The WCV from the higher resolution mesh, denoted as $\mathbf{w}^h_{(i,j)}$, is the vector from the midpoint of the support edge $\mathbf{e}_{(i,j)}$ in the initial resolution mesh to the newly added vertex. For example, as shown in Fig. 6, the WCVs $\mathbf{w}^h_{(2,3)}$, $\mathbf{w}^h_{(2,4)}$ and $\mathbf{w}^h_{(3,4)}$ are associated to the support edge vectors, $\mathbf{e}_{(2,3)}$, $\mathbf{e}_{(2,4)}$ and $\mathbf{e}_{(3,4)}$, from the initial resolution mesh. We use the WCVs from the higher resolution mesh as one of the geometric features for 3D steganalysis.

The edge vector in the higher resolution mesh, $\mathbf{e}^h_{(i,j)}$, is also considered as a geometric feature. An example of edge vector in the higher resolution mesh is $\mathbf{e}^h_{(9,15)}$ in Fig. 6,

Two geometric features, $\beta_{(i,j)}$ and $\rho^h_{(i,j)}$, which are analogue to $\alpha_{(i,j)}$ and $\rho^l_{(i,j)}$ from the lower resolution mesh, are obtained from the higher resolution mesh. $\beta_{(i,j)}$ is the angle between $\mathbf{w}^h_{(i,j)}$, and its support edge vector, $\mathbf{e}_{(i,j)}$ from the initial resolution mesh, which is calculated in a similar way to equation (1). For instance, $\beta_{(3,9)}$ shown in Fig. 6, is the angle between $\mathbf{w}^h_{(3,9)}$ and $\mathbf{e}_{(3,9)}$. Meanwhile, $\rho^h_{(i,j)}$ represents the ratio between the Euclidean norm of the WCV, $\mathbf{w}^h_{(i,j)}$, and that of its support edge vector, $\mathbf{e}_{(i,j)}$, from the initial resolution mesh.

In order to capture the relationship between each WCV and its neighboring WCVs, we consider the average of the neighboring WCVs for each given WCV from the higher resolution mesh. We define that two WCVs are neighbors only when their terminal points are adjacent in the higher resolution mesh. The set of neighboring WCVs of a given WCV $\mathbf{w}^h_{(i,j)}$, is denoted as $\mathcal{N}(\mathbf{w}^h_{(i,j)})$. Then the average neighboring WCVs of $\mathbf{w}^h_{(i,j)}$ is calculated as :

$$\bar{\mathbf{w}}^h_{(i,j)} = \frac{1}{|\mathcal{N}(\mathbf{w}^h_{(i,j)})|} \sum_{\mathbf{w}^h_{(k,l)} \in \mathcal{N}(\mathbf{w}^h_{(i,j)})} \mathbf{w}^h_{(k,l)}, \tag{4}$$

where $|\cdot|$ represents the size of the set. In Fig. 6, $\bar{\mathbf{w}}^h_{(3,4)}$ represents the average of the neighboring WCVs for $\mathbf{w}^h_{(3,4)}$, namely, $\mathbf{w}^h_{(2,4)}$, $\mathbf{w}^h_{(2,3)}$, $\mathbf{w}^h_{(3,9)}$ and $\mathbf{w}^h_{(4,9)}$.

Another feature considered is the difference between the WCV and the average of its neighboring WCVs :

$$\mathbf{w}^h_{(i,j)}{}' = \mathbf{w}^h_{(i,j)} - \bar{\mathbf{w}}^h_{(i,j)}. \tag{5}$$

Meanwhile, another geometric feature is the angle between the WCV and the average of its neighboring WCVs :

$$\theta_{(i,j)} = \arccos\left(\frac{\mathbf{w}^{\mathrm{h}}_{(\mathrm{i,j})} \cdot \bar{\mathbf{w}}^{\mathrm{h}}_{(\mathrm{i,j})}}{\|\mathbf{w}^{\mathrm{h}}_{(\mathrm{i,j})}\| \cdot \|\bar{\mathbf{w}}^{\mathrm{h}}_{(\mathrm{i,j})}\|}\right), \tag{6}$$

where $\bar{\mathbf{w}}^h_{(i,j)}$ is provided in (4).

Table 1: A list of the geometric features derived from the 3D wavelet multiresolution analysis.

Index	Notation	Geometrical representation	Type	Resolution
1	$\mathbf{e}_{(i,j)}$	Edge vector	Vector	Initial
2	$\mathbf{e}^*_{(i,j)}$	Flipped edge vector	Vector	Initial
3	$\mathbf{w}^l_{(i,j)}$	Wavelet coefficient vector (WCV)	Vector	Lower
4	$\mathbf{e}^l_{(i,j)}$	Edge vector	Vector	Lower
5	$\alpha_{(i,j)}$	Angle between $\mathbf{w}^l_{(i,j)}$ and $\mathbf{e}^l_{(i,j)}$	Scalar	Lower
6	$\rho^l_{(i,j)}$	Ratio between $\|\mathbf{w}^l_{(i,j)}\|$ and $\|\mathbf{e}^l_{(i,j)}\|$	Scalar	Lower
7	$\mathbf{w}^h_{(i,j)}$	WCV	Vector	Higher
8	$\mathbf{e}^h_{(i,j)}$	Edge vector	Vector	Higher
9	$\beta_{(i,j)}$	Angle between $\mathbf{w}^h_{(i,j)}$ and $\mathbf{e}_{(i,j)}$	Scalar	Higher
10	$\rho^h_{(i,j)}$	Ratio between $\|\mathbf{w}^h_{(i,j)}\|$ and $\|\mathbf{e}_{(i,j)}\|$	Scalar	Higher
11	$\bar{\mathbf{w}}^h_{(i,j)}$	Averaged neighboring WCV	Vector	Higher
12	$\mathbf{w}^h_{(i,j)}{}'$	Difference between $\mathbf{w}^h_{(i,j)}$ and $\bar{\mathbf{w}}^h_{(i,j)}$	Vector	Higher
13	$\theta_{(i,j)}$	Angle between $\mathbf{w}^h_{(i,j)}$ and $\bar{\mathbf{w}}^h_{(i,j)}$	Scalar	Higher
14	$\mu^M_{(i,j)}$	Mean of the angles between WCV and its neighboring WCVs	Scalar	Higher
15	$\mu^V_{(i,j)}$	Variance of the angles between WCV and its neighboring WCVs	Scalar	Higher
16	$\kappa^M_{(i,j)}$	Mean of the differences between the norms of WCV and its neighboring WCVs	Scalar	Higher
17	$\kappa^V_{(i,j)}$	Variance of the differences between the norms of WCV and its neighboring WCVs	Scalar	Higher

For each WCV from the higher resolution mesh, we consider the mean and variance of the angles between the WCV and its neighboring WCVs as geometric features. These are given by the following formulae:

$$\mu^M_{(i,j)} = \frac{1}{|\mathcal{N}(\mathbf{w}^h_{(i,j)})|} \sum_{\mathbf{w}^h_{(k,l)} \in \mathcal{N}(\mathbf{w}^h_{(i,j)})} \delta_{(k,l)}, \tag{7}$$

$$\mu^V_{(i,j)} = \frac{1}{|\mathcal{N}(\mathbf{w}^h_{(i,j)})|} \sum_{\mathbf{w}^h_{(k,l)} \in \mathcal{N}(\mathbf{w}^h_{(i,j)})} \left(\delta_{(k,l)} - \mu^M_{(i,j)}\right)^2, \tag{8}$$

where $\delta_{k,l}$ is the angle between $\mathbf{w}^h_{(i,j)}$ and its neighboring WCV, $\mathbf{w}^h_{(k,l)} \in \mathcal{N}(\mathbf{w}^h_{(i,j)})$:

$$\delta_{(k,l)} = \arccos\left(\frac{\mathbf{w}^h_{(i,j)} \cdot \mathbf{w}^h_{(k,l)}}{\left\|\mathbf{w}^h_{(i,j)}\right\| \cdot \left\|\mathbf{w}^h_{(k,l)}\right\|}\right) \tag{9}$$

We also consider the mean and variance of the absolute differences between the Euclidean norms of each WCV and its neighboring WCVs, namely :

$$\kappa^M_{(i,j)} = \frac{1}{|\mathcal{N}(\mathbf{w}^h_{(i,j)})|} \sum_{\mathbf{w}^h_{(k,l)} \in \mathcal{N}(\mathbf{w}^h_{(i,j)})} \left| \|\mathbf{w}^h_{(i,j)}\| - \|\mathbf{w}^h_{(k,l)}\| \right|, \tag{10}$$

$$\kappa^V_{(i,j)} = \frac{1}{|\mathcal{N}(\mathbf{w}^h_{(i,j)})|} \sum_{\mathbf{w}^h_{(k,l)} \in \mathcal{N}(\mathbf{w}^h_{(i,j)})} \left(\|\mathbf{w}^h_{(k,l)}\| - \kappa^M_{(i,j)} \right)^2 . \tag{11}$$

4.4. Defining the discriminating feature vectors

All the features proposed in this research study, derived using the 3D wavelet multiresolution analysis framework, are listed in Table 1, where their notation is indicated together with their geometrical representation and the mesh resolution level used for their calculation. The geometric features of the original mesh as well as for the smoothed one are extracted simultaneously and then subtracted from each other. It can be observed from Table 1 that 8 of the proposed geometric features are vectors while the other 9 are scalars.

For the scalar geometric features, we consider the absolute differences between the geometric feature from the original mesh, denoted as g_t, and that from the smoothed mesh, g'_t :

$$\phi_t = |g_t - g'_t|. \tag{12}$$

where t is the index of the geometric feature.

The difference between the geometric features defined as vectors $\mathbf{g}_t$, from the original mesh, and from the smoothed mesh, $\mathbf{g}'_t$ are calculated in four different ways. Firstly, the absolute differences are calculated for features defined in the Cartesian coordinate system, such as

$$\begin{aligned} \phi_{t_1} &= |\mathbf{g}_{t,x} - \mathbf{g}'_{t,x}|, \\ \phi_{t_2} &= |\mathbf{g}_{t,y} - \mathbf{g}'_{t,y}|, \\ \phi_{t_3} &= |\mathbf{g}_{t,z} - \mathbf{g}'_{t,z}|, \end{aligned} \tag{13}$$

where $\mathbf{g}_{t,x}$ represents the x-component of the vector $\mathbf{g}_t$ in the Cartesian coordinate system. Secondly, the norm of the difference between vectors $\mathbf{g}_t$ and $\mathbf{g}'_t$ is calculated as

$$\phi_{t_4} = \|\mathbf{g}_t - \mathbf{g}'_t\|, \tag{14}$$

and we also consider the absolute differences between the norms of the two vectors, namely,

$$\phi_{t_5} = | \, \|\mathbf{g}_t\| - \|\mathbf{g}'_t\| \, |. \tag{15}$$

Eventually, the angle between the two vectors, $\mathbf{g}_t$ and $\mathbf{g}'_t$ is considered as well,

$$\phi_{t_6} = \arccos \left(\frac{\mathbf{g}_{\mathrm{t}} \cdot \mathbf{g}'_{\mathrm{t}}}{\|\mathbf{g}_{\mathrm{t}}\| \cdot \|\mathbf{g}'_{\mathrm{t}}\|} \right). \tag{16}$$

The differences between the geometric features from the original mesh and those of the smoothed one are summarized into a set of $8 \times 6 + 9 = 57$ elements, $\mathbf{\Phi} = \{\phi_t | t = 1, 2, \ldots, 57\}$. In order to introduce evenness in the feature distribution representation, we calculate the logarithm for each entry of $\mathbf{\Phi}$. Finally, we consider the first four statistical moments, representing the mean, variance, skewness and kurtosis, of $\{\lg(\phi_t) | \phi_t \in \mathbf{\Phi}\}$ resulting into a $57 \times 4 = 228$ dimensional feature vector $\mathbf{X}$. The feature vector $\mathbf{X} = [x_1, x_2, \ldots, x_{228}]$ and the class label y, corresponding to the mesh $\mathcal{O}$, are used as inputs to a machine learning algorithm in order to train the 3D steganalyzer. The proposed 228-dimensional 3D Wavelet Feature Set is labeled as WFS228.

From Table 1 we can observe that there are more features extracted from the higher resolution mesh than from the lower resolution mesh. This is due to the uncertainty arising when grouping the triangles forming mesh neighborhoods, during the implementation of the 3D wavelet decomposition, due to the difficulty to predict which WCVs are the neighbors for a certain WCV from a lower resolution mesh. The geometric features that would represent the information of the neighboring WCVs, indexed as 11-17 in Table 1, can not be extracted from the lower resolution mesh. Moreover, the features extracted from the higher resolution mesh may have linear dependencies to some extent, because the location of the vertex in the higher resolution mesh relies on a linear combination of the vertices in the Butterfly neighborhood from the original resolution mesh.

5. Experimental results

In the following we evaluate the performance of the proposed WFS228 feature set by aiming to detect the information embedded by eight 3D information hiding algorithms. Meanwhile, we compare the results with the performance provided by four other 3D steganalytic feature sets. We consider 354 cover-meshes from the Princeton Mesh Segmentation project [42] database, for the experiments. These meshes represent various shapes including that of the human body, animals, statues, tools and so on.

The features are extracted from the cover-meshes and the corresponding stego-meshes when embedded with information by various 3D embedding algorithms. During the preprocessing stage, we firstly apply the Laplacian smoothing once on both cover-meshes and stego-meshes, by setting the scale factor as $\lambda = 5$ as in [34]. The 3D steganalytic features are extracted as described in Section 4. We consider the proposed feature set WFS228, and compare its results against other 3D steganalytic feature sets such as: YANG208 [30], LFS52 [32], LFS64 [33] and LFS76 [34]. We can observe that while LFS76 features [34] represent the statistics of a variety of local geometric properties for surfaces and their interconnected vertices, WFS228 models relationships between regions at different scales of object's surface. Considering the complementarity of their representations, we combine LFS76 and the proposed WFS228 while aiming to identify the information embedded by a variety of information hiding algorithms. The parameters used for the calculation of YANG208, LFS52, LFS64 and LFS76 are identical to those used in [34].

The steganalyzers are trained using the Fisher Linear Discriminant (FLD) ensemble which is broadly used for image steganalysis as well [43, 44, 45, 46, 47]. The FLD ensemble includes a number of base learners trained uniformly on feature sets, which are randomly sampled from the whole data set. The FLD ensemble uses the majority voting to combine the results of all base learners, resulting in a much higher accuracy than any individual base learner [44, 48].

For each steganalyzer, we split the 354 pairs of cover-meshes and stego-meshes into 260 pairs used for training and 94 pairs for testing. The steganalysis results are assessed by calculating the median value of the areas under the Receiver Operating Characteristic (ROC) curves of the testing results, evaluated for 30 different data splits into training and testing sets.

5.1. Steganalysis when considering stego-meshes produced by 3D wavelet-based information hiding algorithms

We firstly test the steganalytic features' performance when detecting the secret information embedded by the Wavelet-based High Capacity (WHC) watermarking method and Wavelet-based FRagile (WFR) watermarking method, proposed in [24]. When implementing each of these watermarking algorithms, the information is hidden into meshes after one iteration of the 3D wavelet decomposition, rather than hierarchically as described in [24]. In order to assess the influence of various parameters influencing WHC, we consider the control parameter as $\epsilon_{hc} \in \{50, 100, 500, 1000\}$. Meanwhile, the quantization step for WFR is set to $\Delta_\theta \in \{\pi/6, \pi/4, \pi/3, \pi/2\}$. The other parameters used for WHC and WFR are all identical to the those used in [24].

Typical ROC curves for the 3D steganalysis results when the information was embedded by WHC ($\epsilon_{hc} = 100$) and WFR ($\Delta_\theta = \pi/3$) when using the FLD ensembles trained on various 3D steganalytic feature sets are shown in Fig. 7. Instead of presenting many ROC curves, Fig. 8 contains the median values of the area under the ROC curve showing the detection results for stego-meshes carrying the information hidden by either WHC or WFR, when varying the values of their characteristic parameters, ϵ_{hc} and Δ_θ during 30 trials. In addition, Fig. 9 provides the box plots, showing the confidence intervals, for the area under the ROC curve of the stego-meshe detection, when watermarked by either WHC or WFR, and when modifying the characteristic embedding parameters for the information hidding algorithm.

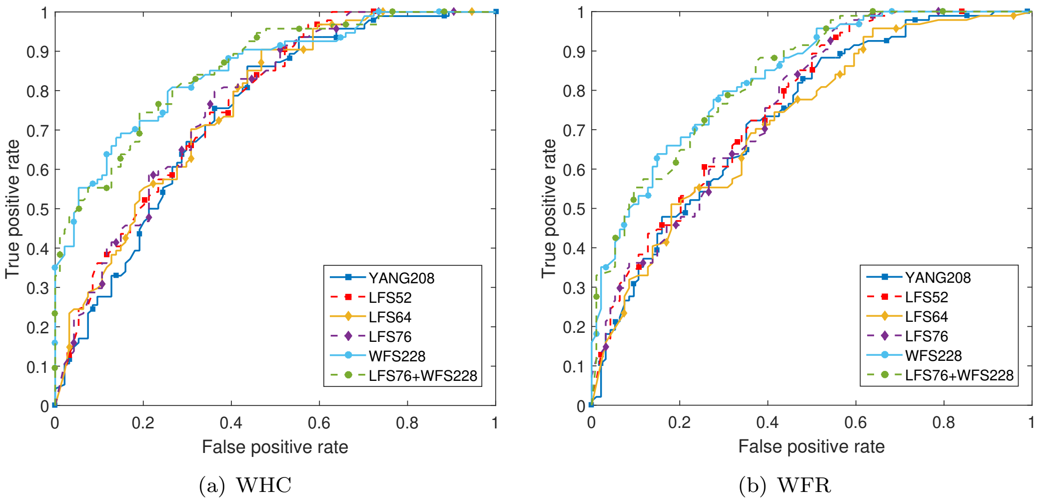

(a) WHC (b) WFR

Figure 7: ROC curves corresponding to the steganalysis results when using the FLD ensembles trained on various 3D steganalytic feature sets, considering that WHC ($\epsilon_{hc} = 100$) and WFR ($\Delta_\theta = \pi/3$) were used for embedding information.

It can be observed from Figures 7, 8 and 9 that the proposed feature set, WFS228, and the combination of LFS76 and WFS228 have better performance than any of the other 3D steganalytic feature sets. Moreover, it is evident from Fig. 8 that the area under the ROC curves increases from around 0.8 to 0.85, by using WFS228 instead of LFS76, resulting in about 6% improvement. Among the existing feature sets, LFS76 shows relatively better performance than YANG208, LFS52 and LFS64, but not as good as WFS228. It can be inferred that the 24 features extracted using the localized spherical coordinates of the mesh contribute to the advantages of using LFS76 when comparing with the results provided by LFS52. It is noted that, although LFS64 also includes LFS52 as a subset, its performance is usually worse than the latter, which means that the additional features in LFS64, such as the edge normal, mean curvature and total curvature are not that efficient, when targeting the hidden information embedded by either WHC or WFR. It can also be observed from Fig. 8(a) that when ϵ_{hc} increases, the accuracy of the steganalyzers trained using the feature set WFS228 and the combination of LFS76 and WFS228, would decline. This happens because increasing ϵ_{hc} leads to a smaller quantization step during embedding, and subsequently a lower level of embedding distortion. According to the results from Fig. 8(b), the parameter Δ_θ doesn't affect the embedding distortion for WFR.

5.2. 3D steganalysis, when the information is hidden by other information hiding algorithms

In the following we consider identifying the 3D stego-meshes produced by hiding information using six different embedding algorithms, which do not use the 3D wavelet transform during the embedding. These algorithms are: the 3D steganography algorithm proposed in [14] based on the Hamiltonian Path Quantization (HPQ) and its improved version which was specifically designed to resist at 3D steganalysis, called HPQ-R [4]; the Multi-Layer Steganography (MLS) proposed in [11]; two blind robust watermarking algorithms which modify either the mean or the variance of the distribution of the vertices' radial distances in the Spherical Coordinate System, denoted as MRS and VRS, from [7], and the Steganalysis-Resistant Watermarking (SRW) method proposed in [10].

For both 3D steganographic algorithms, HPQ and HPQ-R, the interval parameter is set as $\Delta = 1 \times 10^{-7}$ and the relative payload is set at 24 Bits Per Vertex (BPV), as in [4]. When considering the MLS information hidding method from [11], we set the number of layers to 10, and the number of intervals as 10,000. During the information embedding, all the vertices in the mesh are used as payload carriers, except for three vertices which are used as references for the extraction process. So the relative payload embedded by MLS is 10 BPV. For MRS and VRS watermarking methods from [7], we consider $\alpha = 0.04$ for the watermark strength while

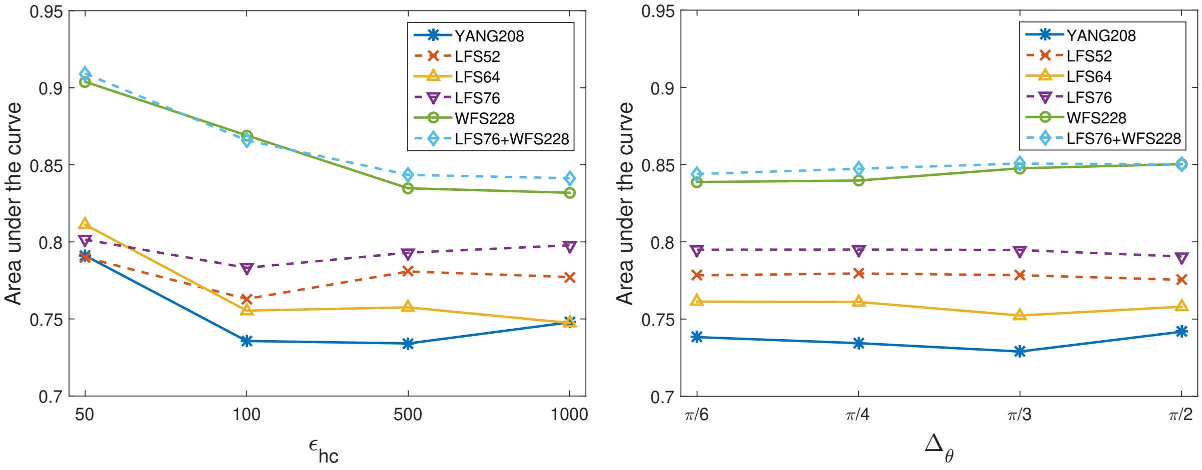

(a) WHC (b) WFR

Figure 8: Median values of the area under the ROC curve for steganalysis detection results calculated over 30 independent splits when the information was hidden using WHC and WFR steganography algorithms. The parameters characterizing the embeddings are varied, as shown on the scales of X axes for the plots.

fixing the incremental step size to $\Delta k = 0.001$ and the message payload as 64 bits. During the generation of the stego-meshes using the SRW method from [10], we set the parameter $K = 128$ which determines the number of bins in the histogram of the radial distances for all vertices. According to [10], the upper bound of the embedding capacity is $\lfloor (K-2)/2 \rfloor$ bits. The parameter that controls the trade-off between watermarking robustness and distorsion for SRW is n_{thr}, which is set as 20.

The plots from Fig. 10 show the results for the area under the ROC curve for the detection results for the steganalyzers using various feature sets, when testing over 30 independent data set splits and considering the information embedded by the above-mentioned six 3D information embedding algorithms. We can observe from Fig. 10 that the combination of LFS76 and WFS228 achieves the best performance for the steganalysis of the stego-meshes embedded by these six 3D information hiding algorithms. The correlation between the feature sets WFS228 and LFS76 is very limited, given that they represent completely different 3D shape properties. The WFS228 feature set, when compared to LFS76, can capture complementary information about the existence of hidden information in 3D objects, represented as meshes, from the relationships between surfaces of different scales through multiresolution wavelet analysis of mesh surfaces. Given their properties, WFS228 features can identify the embedded secret information even when the secret message is not actually embedded in the 3D wavelet domain of the objects. For example, the WFS228 feature set can identify the displacement of the vertices along the direction of the mesh edges, which was the approach employed by the recently proposed HPQ-R embedding algorithm [4], while the other steganalytic feature sets would fail to capture such changes, as it can be observed from Fig. 10(b). Moreover, the WFS228 feature set calculation considers a larger vertex neighborhood than LFS76, when using the Butterfly scheme, in order to generate the higher resolution mesh. Consequently, the proposed feature set can capture the embedded shape distortions from a larger region than in the case of the other 3D feature sets. We can also observe that LFS64 provides slightly worse performance than LFS52 with respect to the steganalysis of the stego-meshes embedded by HPQ, HPQ-R and MLS, but better performance than in the case of the information hidden by the MRS, VRS and SRW algorithms. We infer that the additional 12-dimensional features in LFS64, proposed in [33], are more sensitive to larger distortions, because MRS, VRS and SRW are robust watermarking algorithms which usually would produce larger distortions than other 3D steganographic algorithms, such as HPQ, HPQ-R or MLS.

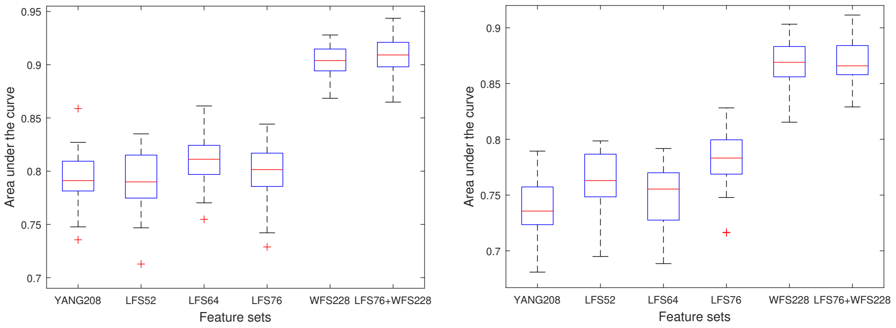

(a) WHC ($\epsilon_{hc} = 50$) (b) WHC ($\epsilon_{hc} = 100$)

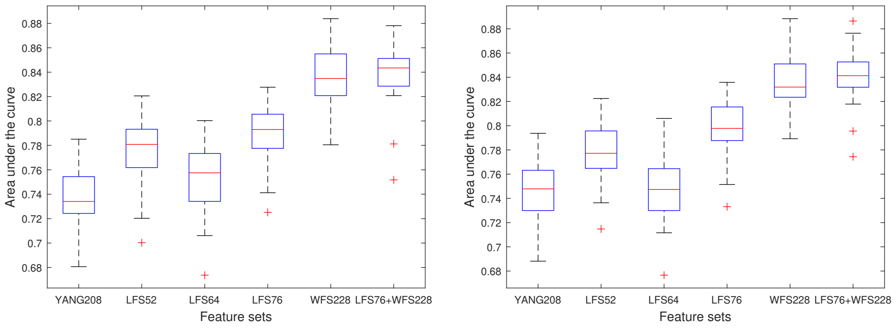

(c) WHC ($\epsilon_{hc} = 500$) (d) WHC ($\epsilon_{hc} = 1000$)

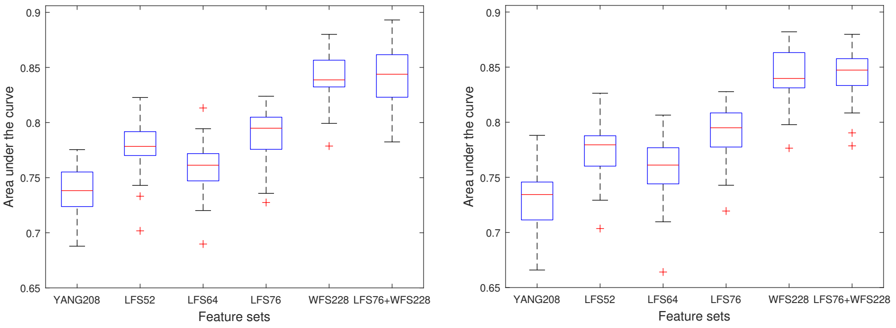

(e) WFR ($\Delta_\theta = \pi/6$) (f) WFR ($\Delta_\theta = \pi/4$)

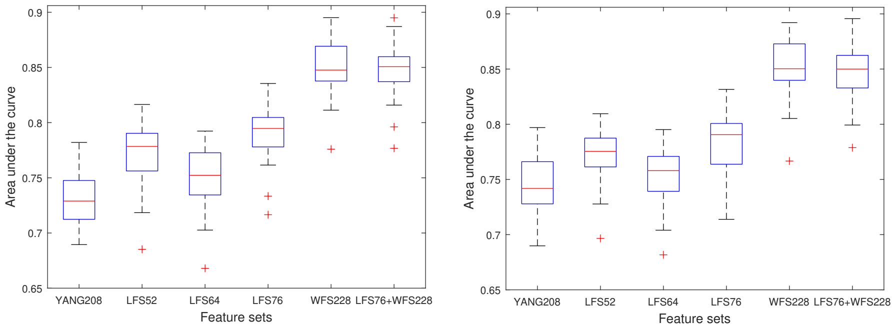

(g) WFR ($\Delta_\theta = \pi/3$) (h) WFR ($\Delta_\theta = \pi/2$)

Figure 9: Box plots showing the confidence intervals for the area under the ROC curve of the detection results for the steganalyzers trained when testing over 30 independent splits for WHC and WFR, when considering various values for the parameters characterizing the information embedding algorithms.

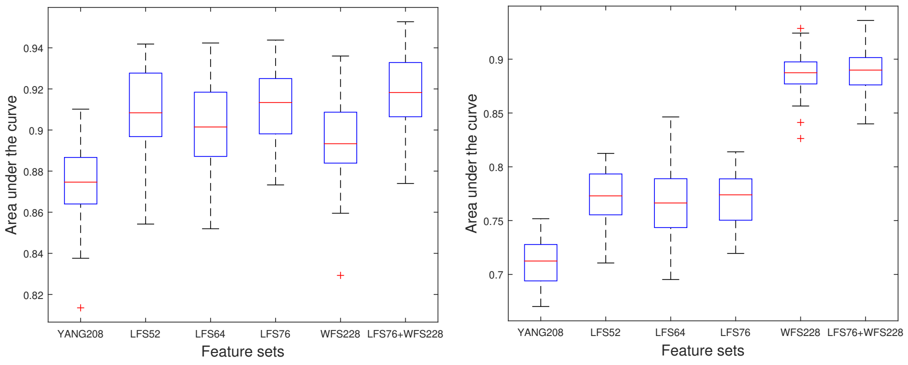

(a) HPQ [14] (b) HPQ-R [4]

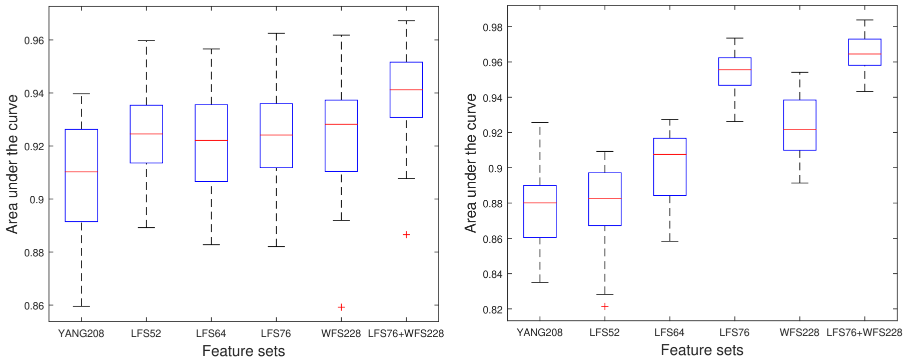

(c) MLS [11] (d) MRS [7]

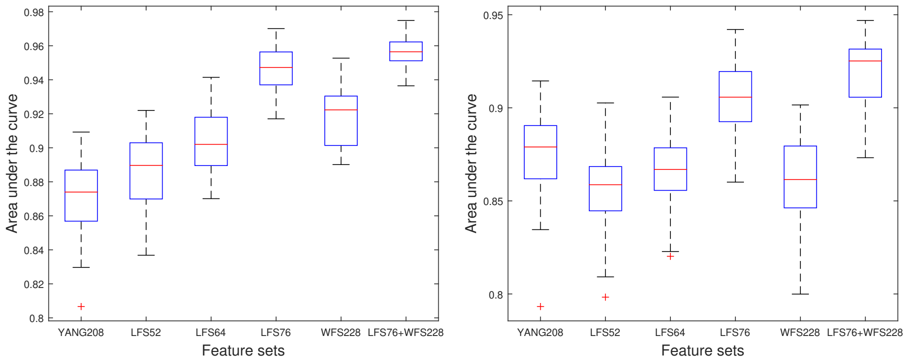

(e) VRS [7] (f) SRW [10]

Figure 10: Box plots showing the confidence intervals for the area under the ROC curve for the detection results of the steganalyzers trained when testing over 30 independent splits for the six 3D information embedding algorithms which do not rely on 3D wavelet analysis for their embeddings.

5.3. Efficiency analysis of the proposed features

In the following we analyze the efficiency of categories the steganalytic features. The features are grouped in various categories according to the type of geometric property they are characterizing. The efficiency of the features is assessed by the relevance score between the feature vectors and the class label, which is calculated by the Pearson correlation coefficient

$$\rho(x_i, y) = \frac{cov(x_i, y)}{\sigma_{x_i}\sigma_y} \tag{17}$$

where x_i is the i-th feature of the given feature set, and y is the class label indicating whether the mesh is a cover-mesh or a stego-mesh, cov represents the covariance and σ_{x_i} is the standard deviation of x_i. The Pearson correlation coefficient is a measure of the linear dependence between two variables which is used for assessing the features' efficiency in classical feature selection algorithms [49, 50]. We make the assumption that a higher linear dependence, or a higher relevance, between the feature and the class label can result in a better discriminant ability of that feature between the classes. So the relevance $\rho(x_i, y)$, is an estimation of the i-th feature's efficiency for 3D steganalysis.

In the following, the features from the set WFS228 are split into 17 categories according to their characteristic representation of the geometric features listed in Table 1. Firstly, the relevance of each feature from the set WFS228 is calculated according to equation (17). Then, the relevance of each category is obtained by averaging the relevances for all the features belonging to that category. The analysis is based on the features extracted from the 354 cover-meshes and their corresponding stego-meshes obtained by embedding information when using the eight information hiding algorithms which have been assessed in Sections 5.1 and 5.2. During these tests we consider the parameters for WHC and WFR as $\epsilon_{hc} = 100$ and $\Delta_\theta = \pi/3$, respectively. The parameters in the other six algorithms, HPQ, HPQ-R, MLS, MRS, VRS and SRW, are the same with the ones used in Section 5.2. Given that various embedding algorithms produce different kinds of distortions in 3D shapes, the relevance of each feature may depend on the information hiding algorithm used for embedding the changes in the 3D shapes.

The relevances for different categories of features in WFS228 are provided in Fig. 11, when considering embedding information in 3D objects by 8 different information hidding algorithms. The categories are indexed according to the geometric feature categories from Table 1. It can be observed from Fig. 11 that features from the categories 5, 6, 9, 10, 13, 14 and 15 have relatively higher relevance with respect to the class label than the other categories. These features are all characterizing the relationships between the WCV and its support edge or the relationships between the WCV and its neighboring WCVs in the higher resolution mesh. Besides, the features from categories 3 and 7, characterizing the geometry of the WCVs, have a similar relevance to the average of the relevances of all classes of features, when steganalysing the information embedded by each of the eight information hiding algorithms. However, the features from categories 1, 2, 4 and 8, representing the edge vectors or flipped edge vectors of meshes from three resolution levels, show a lower relevance than the average. We infer that this is happening because the modifications made by the embedding algorithms are not changing directly the edges in different resolution meshes, so the corresponding features are not so efficient for steganalysis as the others. However, when we train the steganalyzers without the features from categories 1, 2, 4 and 8, the steganalysis results degrade to some extent, which means that all these features are contributing to 3D steganalysis.

6. Conclusion

In this research study, we propose a steganalytic approach for 3D objects, represented as meshes, based on the 3D wavelet multiresolution analysis. Geometric specific features are extracted from the original mesh and its smoothed counterpart, by considering three levels of resolution: the given mesh, a lower resolution and a higher resolution. The lower and the higher resolution meshes are derived from the given mesh using 3D wavelet transformations. The differences between the features extracted from the original mesh and its smoothed version are evaluated. The first four moments of the distributions of the logarithms for these differences are then used to form the proposed 228-dimensional steganalytic feature set, which

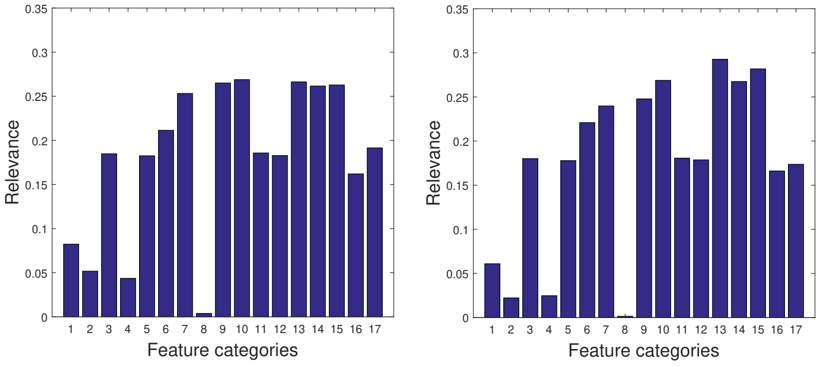

(a) WHC [24] (b) WFR [24]

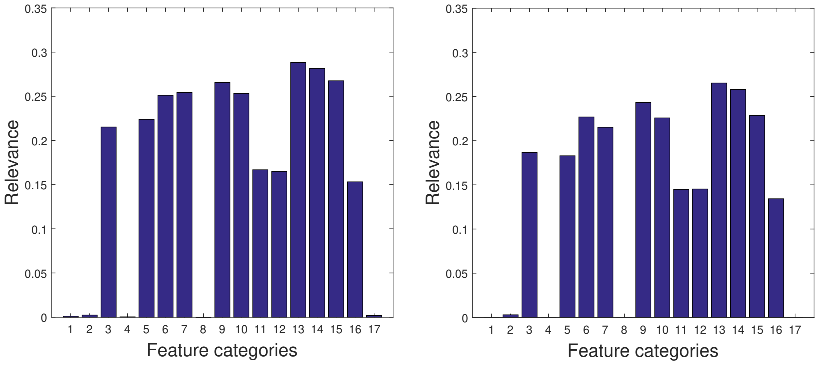

(c) HPQ [14] (d) HPQ-R [4]

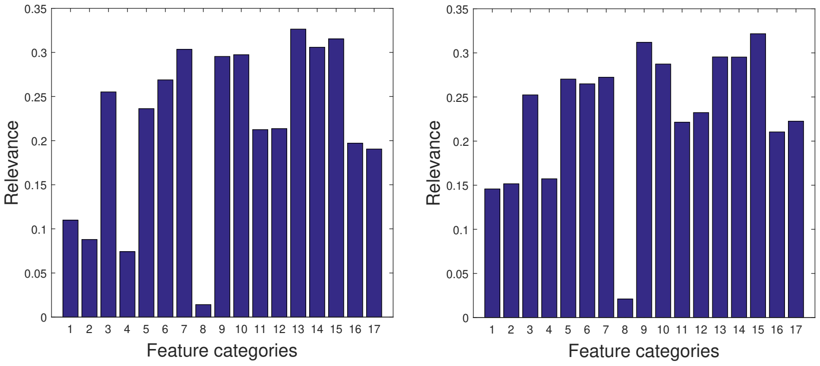

(e) MLS [11] (f) MRS [7]

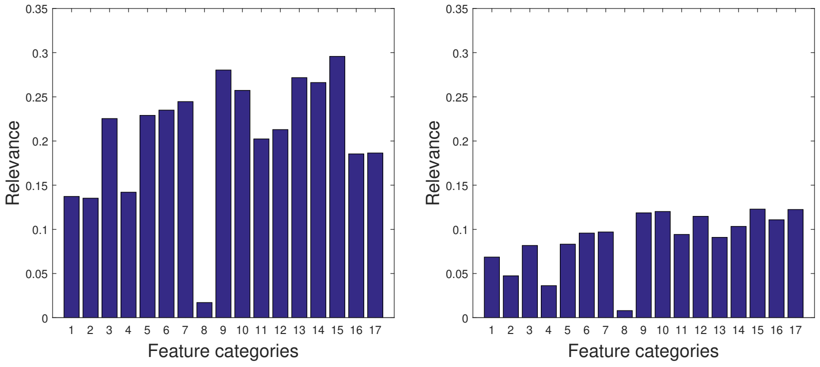

(g) VRS [7] (h) SRW [10]

Figure 11: The relevance between categories of features and class label, where the stego-meshes are obtained using eight different information hiding methods: WHC, WFR, HPQ, HPQ-R, MLS, MRS, VRS and SRW. The labels of the features' categories correspond to the indices of the geometric features from Table 1.

is named WFS228. The experimental results show that the proposed 3D wavelet feature set provides the best results for the steganalysis of the embeddings made by two 3D wavelet-based watermarking algorithms. Furthermore, the combination of LFS76 and the proposed WFS228 achieves better performance than other existing 3D steganalysis features when analyzing the information embedded by six other 3D embedding algorithms. An analysis of the efficiency for various categories of 3D features, derived using 3D wavelet multiresolution analysis, and grouped based on their geometry modelling characteristics, is undertaken in this paper as well.

References

[1] A. Maglo, G. Lavoué, F. Dupont, C. Hudelot, 3D mesh compression: Survey, comparisons, and emerging trends, ACM Computing Surveys (CSUR) 47 (3) (2015) 44.

[2] Dell SecureWorks Counter Threat Unit Threat Intelligence, Stegoloader: A Stealthy Information Stealer, `https://www.secureworks.com/research/stegoloader-a-stealthy-information-stealer`, accessed: 2019-11-01.

[3] B. Stone-Gross, Malware Analysis of the Lurk Downloader, `https://www.secureworks.com/research/malware-analysis-of-the-lurk-downloader`, accessed: 2019-11-01.

[4] Z. Li, S. Beugnon, W. Puech, A. G. Bors, Rethinking the high capacity 3D steganography: Increasing its resistance to steganalysis, in: Proc. IEEE Int. Conf. on Image Processing, 2017, pp. 510–514.

[5] R. Ohbuchi, H. Masuda, M. Aono, Embedding data in 3D models, in: Interactive Distributed Multimedia Systems and Telecommunication Services, 1997, pp. 1–10.

[6] F. Cayre, B. Macq, Data hiding on 3-D triangle meshes, IEEE Transactions on Signal Processing 51 (4) (2003) 939–949.

[7] J.-W. Cho, R. Prost, H.-Y. Jung, An oblivious watermarking for 3-D polygonal meshes using distribution of vertex norms, IEEE Transactions on Signal Processing 55 (1) (2007) 142–155.

[8] M. Luo, A. G. Bors, Surface-preserving robust watermarking of 3-D shapes, IEEE Transactions on Image Processing 20 (10) (2011) 2813–2826.

[9] A. G. Bors, M. Luo, Optimized 3D watermarking for minimal surface distortion, IEEE Transactions on Image Processing 22 (5) (2013) 1822–1835.

[10] Y. Yang, R. Pintus, H. Rushmeier, I. Ivrissimtzis, A 3D steganalytic algorithm and steganalysis-resistant watermarking, IEEE Transactions on Visualization and Computer Graphics 23 (2) (2017) 1002–1013.

[11] M.-W. Chao, C.-h. Lin, C.-W. Yu, T.-Y. Lee, A high capacity 3D steganography algorithm, IEEE Transactions on Visualization and Computer Graphics 15 (2) (2009) 274–284.

[12] P. Amat, W. Puech, S. Druon, J.-P. Pedeboy, Lossless 3D steganography based on MST and connectivity modification, Signal Processing: Image Communication 25 (6) (2010) 400–412.

[13] V. Itier, W. Puech, G. Gesquière, J.-P. Pedeboy, Joint synchronization and high capacity data hiding for 3D meshes, in: SPIE/IS&T Electronic Imaging, 2015, pp. 9393, 05–15.

[14] V. Itier, W. Puech, High capacity data hiding for 3D point clouds based on static arithmetic coding, Multimedia Tools and Applications 76 (24) (2017) 26421–26445.

[15] M. Lounsbery, T. D. DeRose, J. Warren, Multiresolution analysis for surfaces of arbitrary topological type, ACM Transactions on Graphics 16 (1) (1997) 34–73.

[16] H. S. Abdul-Rahman, X. J. Jiang, P. J. Scott, Freeform surface filtering using the lifting wavelet transform, Precision Engineering 37 (1) (2013) 187–202.

[17] F. Payan, M. Antonini, Mean square error approximation for wavelet-based semiregular mesh compression, IEEE Transactions on Visualization and Computer Graphics 12 (4) (2006) 649–657.

[18] A. Kammoun, F. Payan, M. Antonini, Sparsity-based optimization of two lifting-based wavelet transforms for semi-regular mesh compression, Computers & Graphics 36 (4) (2012) 272–282.

[19] H.-C. Shao, W.-L. Hwang, Y.-C. Chen, A backward wavelet remesher for level of detail control and scalable coding, in: Proc. IEEE Int. Conf. on Image Processing, 2014, pp. 5596–5600.

[20] H. Date, S. Kanai, T. Kishinami, Digital watermarking for 3-D polygonal model based on wavelet transform, in: Proc. ASME Design Engineering Technical Conf., 1999, pp. 12–15.

[21] F. Uccheddu, M. Corsini, M. Barni, Wavelet-based blind watermarking of 3D models, in: Proc. ACM Workshop on Multimedia and Security, 2004, pp. 143–154.

[22] M.-S. Kim, S. Valette, H.-Y. Jung, R. Prost, Watermarking of 3D irregular meshes based on wavelet multiresolution analysis, in: Proc. Int. Workshop on Digital Watermarking, 2005, pp. 313–324.

[23] M.-S. Kim, J.-W. Cho, R. Prost, H.-Y. Jung, Wavelet analysis based blind watermarking for 3-D surface meshes, in: Proc. Int. Workshop on Digital Watermarking, 2006, pp. 123–137.

[24] K. Wang, G. Lavoué, F. Denis, A. Baskurt, Hierarchical watermarking of semiregular meshes based on wavelet transform, IEEE Transactions on Information Forensics and Security 3 (4) (2008) 620–634.

[25] A. O. Zaid, M. Hachani, W. Puech, Wavelet-based high-capacity watermarking of 3-D irregular meshes, Multimedia Tools and Applications 74 (15) (2015) 5897–5915.

[26] B. Chen, G. W. Wornell, Quantization index modulation: A class of provably good methods for digital watermarking and information embedding, IEEE Transactions on Information Theory 47 (4) (2001) 1423–1443.

[27] Y.-M. Cheng, C.-M. Wang, A high-capacity steganographic approach for 3D polygonal meshes, The Visual Computer 22 (9-11) (2006) 845–855.

[28] A. Bogomjakov, C. Gotsman, M. Isenburg, Distortion-free steganography for polygonal meshes, Computer Graphics Forum 27 (2) (2008) 637–642.

[29] N.-C. Huang, M.-T. Li, C.-M. Wang, Toward optimal embedding capacity for permutation steganography, Signal Processing Letters, IEEE 16 (9) (2009) 802–805.

[30] Y. Yang, I. Ivrissimtzis, Mesh discriminative features for 3D steganalysis, ACM Transactions on Multimedia Computing, Communications, and Applications 10 (3) (2014) 27:1–27:13.

[31] Y. Yang, I. Ivrissimtzis, Polygonal mesh watermarking using Laplacian coordinates, Computer Graphics Forum 29 (5) (2010) 1585–1593.

[32] Z. Li, A. G. Bors, 3D mesh steganalysis using local shape features, in: Proc. IEEE Int. Conf. on Acoustics, Speech and Signal Processing, 2016, pp. 2144–2148.

[33] D. Kim, H.-U. Jang, H.-Y. Choi, J. Son, I.-J. Yu, H.-K. Lee, Improved 3D mesh steganalysis using homogeneous kernel map, in: Proc. Int. Conf. on Information Science and Applications, 2017, pp. 358–365.

[34] Z. Li, A. G. Bors, Steganalysis of 3D objects using statistics of local feature sets, Information Sciences 415-416 (2017) 85–99.

[35] Z. Li, A. G. Bors, Selection of robust features for the cover source mismatch problem in 3D steganalysis, in: Proc. Int. Conf. on Pattern Recognition, 2016, pp. 4256–4261.

[36] T. Pevny, P. Bas, J. Fridrich, Steganalysis by subtractive pixel adjacency matrix, IEEE Transactions on Information Forensics and Security 5 (2) (2010) 215–224.

[37] J. Fridrich, J. Kodovskỳ, V. Holub, M. Goljan, Breaking HUGO–the process discovery, in: Proc. Int. Workshop on Information Hiding, LNCS, vol. 6958, 2011, pp. 85–101.

[38] J. J. Eggers, R. Bauml, R. Tzschoppe, B. Girod, Scalar costa scheme for information embedding, IEEE Transactions on Signal Processing 51 (4) (2003) 1003–1019.

[39] J. Kodovsky, J. J. Fridrich, Calibration revisited, in: Proc. ACM Workshop on Multimedia and Security, 2009, pp. 63–74.

[40] N. Dyn, D. Levine, J. A. Gregory, A butterfly subdivision scheme for surface interpolation with tension control, ACM Transactions on Graphics 9 (2) (1990) 160–169.

[41] S. Kanai, H. Date, T. Kishinami, Digital watermarking for 3D polygons using multiresolution wavelet decomposition, in: Proc. Int. Workshop Geometric Modeling: Fundamentals and Applications, Vol. 5, 1998, pp. 296–307.

[42] X. Chen, A. Golovinskiy, T. Funkhouser, A benchmark for 3D mesh segmentation, ACM Transactions on Graphics 28 (3) (2009) 73:1–73:12.

[43] T. D. Denemark, M. Boroumand, J. Fridrich, Steganalysis features for content-adaptive JPEG steganography, IEEE Transactions on Information Forensics and Security 11 (8) (2016) 1736–1746.

[44] J. Kodovskỳ, J. Fridrich, V. Holub, Ensemble classifiers for steganalysis of digital media, IEEE Transactions on Information Forensics and Security 7 (2) (2012) 432–444.

[45] T. Pevnỳ, A. D. Ker, Towards dependable steganalysis, in: Proc. SPIE/IS&T Electronic Imaging, 2015, pp. 94090I–94090I–14.

[46] W. Tang, H. Li, W. Luo, J. Huang, Adaptive steganalysis based on embedding probabilities of pixels, IEEE Transactions on Information Forensics and Security 11 (4) (2016) 734–745.

[47] S. Tan, H. Zhang, B. Li, J. Huang, Pixel-decimation-assisted steganalysis of synchronize-embedding-changes steganography, IEEE Transactions on Information Forensics and Security 12 (7) (2017) 1658–1670.

[48] R. Cogranne, J. Fridrich, Modeling and extending the ensemble classifier for steganalysis of digital images using hypothesis testing theory, IEEE Transactions on Information Forensics and Security 10 (12) (2015) 2627–2642.

[49] I. Guyon, A. Elisseeff, An introduction to variable and feature selection, Journal of Machine Learning Research 3 (2003) 1157–1182.

[50] L. Yu, H. Liu, Efficient feature selection via analysis of relevance and redundancy, Journal of Machine Learning Research 5 (Oct) (2004) 1205–1224.